



Manufacturing of a metallic 3D framework coated with a bioglass matrix for implant applications

Zakaria Tabia¹, Meriame Bricha¹, Khalil El Mabrouk^{1,*} , and Sébastien Vaudreuil¹

¹ Euromed Research Center, Euromed Engineering Faculty, Euromed University of Fes, Eco- Campus, Meknes Road, 30 030 Fes, Morocco

Received: 6 May 2020

Accepted: 19 September 2020

Published online:

6 October 2020

© Springer Science+Business Media, LLC, part of Springer Nature 2020

ABSTRACT

In a new approach combining additive manufacturing with bioceramics, a metallic 3D porous structure coated with bioactive glass was produced for possible use in orthopedic implants. This approach aims to combine high mechanical properties of the metallic structure with enhanced biological activity. 316L stainless steel (316L-SS) lattice structures were fabricated using selective laser melting. Despite its good mechanical properties, 316L-SS lacks the biofunctionality required to achieve long-term implantation. To be successfully used as biomaterial, these porous 3D lattice structures were thus coated by 58S bioglass through a simple impregnation method. The use of a silica layer was evaluated as possible pretreatment to improve bioglass adhesion. The coated parts are then assessed by scanning electron microscopy coupled with energy-dispersive spectrometry to qualify the coating. Porous sample parts pretreated with a silica layer presented a denser coating structure when compared with untreated porous metallic structures. The bioactivity in SBF medium shows the formation of a uniform apatite layer after 7 days of immersion, producing the bioregeneration capability. This latter, combined with the lightweight framework structure provided by 316-SS, will increase the lifetime of this new generation of orthopedic implants.

Introduction

In clinical medicine, the increasing number of trauma and pathologies in need of organ or tissue transplantation is becoming a serious issue. This trend can

be explained by several factors, such as the aging population and obesity, both of which are considered as direct precursors of osteoarthritis. However, despite the many approaches available such as the autograft, allograft and xenotransplantation, there are still limitations which can lead to implant rejection.

Handling Editor: Annela M. Seddon.

Address correspondence to E-mail: k.elmabrouk@ueuromed.org

Nevertheless, biomaterials and artificial organs are generally advocated in order to reduce pain and improve the quality of life for patients. Total hip replacements (THR) or total knee replacement (TKR) is currently one of the most common health interventions in the world [1]. In the UK, the annual incidence rate of primary total joints has been growing steadily from 1990 to 2000. Current data from the National Joint Registry for England, Wales and Northern Ireland (NJR) indicates that the number of operations for primary total joint replacement is steadily increasing, with 75,366 hip and 76,497 knee procedures performed in 2012 [2]. These numbers reached, respectively, 79,088 and 85,128 for 2013 [1]. This upward trend will continue and is estimated to reach 96,000 and 119,000 in the UK by 2035 [2]. A similar trend is observed in the USA, where an increase of 174% (572,000 patients) is anticipated for primary total hip arthroplasties by 2030. Total knee arthroplasties are projected to increase in the same period by 673% to 3.48 million procedures. It is expected that the worldwide demand for hip revision surgical operations will double by the year 2026, with knee revisions doubling by 2015.

With the increasing number of THR and TKR performed and anticipated, this type of surgery is becoming a significant financial burden for health services worldwide. For example, each primary THR and TKR procedure costs the National Health Service (NHS) more than 7000 dollars [2]. The cost of hip replacement varies from one country to another; the USA has the highest cost, reaching 40 thousand dollars in 2018, while Poland has the lowest, 5 thousand US dollars. Another limitation of the current implants is its limited lifetime, requiring a revision surgery after ten to fifteen years, a duration influenced by the physical conditions of the patient such as age, sex, and body mass index (BMI) [3]. For the USA, the revision rate for total hip arthroplasty reached approximately 17.5% between 1990 and 2002. This rate is expected to increase by 137% between 2005 and 2030 [4].

To overcome such problems, there is need for alternatives which could be lower priced metallic implants of the same mechanical properties that would avoid additional surgery after implantation. One approach relies on additive manufacturing to overcome these existing limitations by designing personalized bone grafts and accurately controlling its geometry and porosity to biomimic bone tissue

[5, 6]. Additive manufacturing (AM), commonly called three-dimensional (3D) printing, enables the production of 3D complex parts through a layer-by-layer process. This permits the double control of external and internal shapes [7].

Human bone possesses a complex 3D architecture with a wide range of porosity, covering nano- to macroscale. This porosity impacts positively osteoinduction and osteoconduction by giving a suitable ECM micro-environment for cell proliferation (nanoscale pore diameter), enabling transport of nutrients and metabolic waste (micrometer pore diameter 150–800 μm) and conducive to new tissue growth and blood vessels formation (ten micrometers pore diameter 10–100 μm) [8, 9]. The ideal bone bio-materials thus must not only mimic the composition and external shape (macro-architecture) of natural bone, it must also correspond to its internal shape (micro-architecture) [10].

Implants manufacturing currently rely on metals, ceramics and polymers, where the choice of material will be influenced by the implant type and desired application. Metallic materials, such as titanium alloys, stainless steel and cobalt–chromium [9, 11, 12], are the most used in load-bearing applications, thanks to their mechanical reliability in comparison with other materials. The high weight and stiffness of metallic implant are two drawbacks hindering their use in orthopedic implants. To address this shortcoming, sizeable research activities are currently investigating ways to achieve significant improvements [13]. Using additive manufacturing (AM) techniques, a number of lattice structures and functionally graded porous scaffolds (FGPS) have been generated and extensively developed [11, 13]. Their high level of controlled porosity enables the achievement of reduced stiffness and weight. This helps avoid the “stress shielding” phenomenon without counteracting the “Wolff’s Law” [13]. With their high specific area, 3D-printed interconnected porous scaffolds have an impressive ability to enhance biological properties, especially osseointegration and new bone tissue in growth [10].

To produce metallic implants using AM, two technologies based on the powder bed fusion principle are currently available. The first one, selective laser melting (SLM), relies on a laser to melt locally a layer of metallic powder. The second, electron beam melting (EBM), uses an electron beam under vacuum to achieve the same results. Because the design of

personalized implant was always a goal to improve healthcare quality, AM was investigated early on. In 2008, the first study was performed by Harrysson et al. on the design and fabrication of tailored implant based on titanium, using the electron beam melting (EBM) method. Three configurations were investigated: hip stems with mesh, hole and solid. Harrysson et al. found good mechanical properties with the fabricated lattice structures, imitating the stiffness of bone and thus decreasing stress shielding and bone remodeling [14]. Murr et al. proposed a variety of knee and hip implants incorporating open-cellular structures (foam and mesh components), produced by EBM from Ti–6Al–4V and Co–29Cr–6Mo alloys. They showed that such implants possess good mechanical and biological properties with regard to stress shielding and bone cell in growth. Such implants have been introduced to humans over the past several years and received European CE certification [15]. However, there are still concerns about the use of metallic materials because of the possible slow release of toxic ions with adverse effects as well as their limited biological activity. Coating the implant with a bioactive layer is one approach to overcome these shortcomings [9, 16, 17]. Hybrid implants can also fulfill this requirement [12]. Fathi et al. prepared using sol–gel technique bioactive glass nanopowder (57.44% CaO, 35.42% SiO₂ and 7.15% P₂O₅ in molar percentages) as coating for 316L-SS implant to simultaneously improve biocompatibility and bone osseointegration [18, 19]. Such sol–gel protective coatings are a good way to enhance the chemical stability and corrosion resistance of metal substrates. Using spray [20], electrophoretic deposition [21], or atomic layer deposition [22–24], good results have been obtained for an array of metals, like steel, aluminum, copper, magnesium and their alloys [12, 25]. The wettability behavior of the coating on the metallic material is a crucial factor in obtaining the bioactivity and biocompatibility properties sought [26]. Pourhashem et al. prepared a double layer of bioglass–silica coatings on 316L stainless steel by sol–gel method. Sample parts immersed 30 days in simulated body fluid (SBF) displayed a growth of amorphous apatite, hydroxyapatite (HA) and CaSiO₃ film on coatings [27]. Despite various studies carried out on the bioactive coating of metal parts, there are few, if any, studies focused on the development of such bioglass coatings on porous 3D structures. A recent study conducted by Yan and San examined the

biocompatibility of hydroxyapatite sol–gel-coated 316L stainless steel implants manufactured by SLM [28]. Bioactivity enhancement from the HA coating was confirmed when compared to the as-printed 316L stainless steel. Multi-materials structures of Ti₆Al₄V were produced by SLM for hip replacement applications, incorporating a step of bioglass 45S5 impregnation. The impregnated samples, having a high wettability and reduced toxic ions release, led to cell growth in an adequate environment [29]. To the best of our knowledge, there is no report of bioglass coating on rhombic dodecahedron lattice structure based on 316L stainless steel printed by SLM technology. As known from the literature, stainless steel 316L presents one of the widely bioinert metals and alloys (titanium alloy Ti–6Al–4 V, Co–Cr alloys, pure titanium and tantalum) used for bone substitutes and orthopedics implants, because it shows practical biocompatibility, and is inexpensive [30]. Furthermore, the crucial advantage of employing stainless steel is its easiness to process by SLM unlike the other metals, as well as its ability to create porous structures with smaller strut thicknesses [31].

In this paper, the stainless steel used as substrates is typically composed of molybdenum, chromium and nickel with balance iron, in addition to the alloying elements to improve the corrosion resistance. It is often reported in the literature that nickel ions are released from stainless steel samples, causing cancer to humans. Gopi et al. [32] and He et al. [33] used two types of 316L stainless steel with different contents of nickel of about 11.65 and 10 wt%, respectively. They both conclude the potential use of the resulted material based on 316L stainless steel as biocompatible in tissue engineering applications. It is clear that the stainless steel used in our study contains more nickel than the aforementioned studies. At the European Union level, they have strictly prohibited the presence of nickel in metal alloys intended for applications such as biomaterials.

The objective of this study is to report on a bioactive coating, based on 58S bioglass, prepared by evaporation-induced self-assembly (EISA) method on 316L stainless steel porous structured implant for orthopedic application, through a simple impregnation technique. Bioactivity testing of these coated porous parts in a simulated biological fluid is presented. The results will help in predicting the behavior of these hybrid 3D porous implants once introduced in human body. The bioactivity of the 3D

porous samples coated with bioglass matrix is expressed by the precipitation of uniform apatite layer after only seven days of immersion period, an evidence of bone bioregeneration.

Materials and Methods

Materials

The stainless steel metallic powder used in this study was purchased from SLM Solutions (Table 1). For the synthesis of the bioactive glass powders and surface coating for the 3D printed samples, the following chemical products were used as received and without any further purification: ethanol (C₂H₆O, 99%), hydrochloric acid (HCl, 37%), triblock copolymer Pluronic L-81 (Mn ~ 2800), tetraethyl orthosilicate (TEOS, Si(OC₂H₅), 99.9%), triethyl phosphate (TEP, (C₂H₅O)₃PO, 99.8%), calcium nitrate tetrahydrate (CaNO₃, 4H₂O, 99%) and nitric acid (65%).

Sample Parts Printing and Surface Pretreatment

The geometrical configuration for the 3D rhombic dodecahedron with a relative density of 20% lattice is illustrated in Fig. 1. A rhombic dodecahedron unit cell is presented in Fig. 1a, b with two different views: “top front left” and “top view”, characterized by a surface and a volume of 995.613 mm² and 79.856 mm³, respectively. Figure 1c, d illustrates the test cube with a lattice thickness t equal to 0,3 mm, used for impregnation testing to evaluate bioglass coating. Test cubes are printed in the same conditions as the hip implant (Fig. 1e, f).

All parts were fabricated using SLM 125 HL machine from SLM Solutions (Germany), equipped with a 400 W fiber laser. Operating conditions were identical for all production jobs, with contouring and volume given in Table 2. The volumetric laser energy density (E_v) was calculated according to Eq. (1) [34]:

$$E_v = \frac{P}{v * h * t} \quad (1)$$

where P in W is the power laser; v is the average scanning speed in mm/s; h is the hatching spacing in mm; and the layer thickness t in mm.

Part production was performed on a stainless steel base plate under a nitrogen atmosphere to reduce the reactivity of the 316L-SS powder. Prior to manufacturing, the location of the parts on the build plate was carefully considered to achieve a uniform heat distribution during fabrication. The build plate, with the parts still attached, was heat-treated at 300 °C for 2H in order to reduce the residual stress. After oven cooling, the parts were removed from the build plate using a horizontal band saw, using lubricating coolant to avoid localized overheating. All samples were cleaned in an ultrasonic bath, with frequent distilled water changes. The last cleaning step is an acetone soaking for 30 min.

To evaluate the effects of surface pretreatment on bioglass coating, some of the stainless steel specimens were coated with a silica layer prior to further processing. The SiO₂ coating sol was prepared as follows: a 70:30 (wt%) mixture of absolute ethanol and deionized water was prepared, after which its pH solution was adjusted to 1.5 using nitric acid. An exact volume of TEOS (26.8 ml) was added dropwise to the mixture solution, which was maintained under stirring until a clear solution is obtained. The 3D printed samples are then slowly immersed in the silica sol and withdrawn after 15 min, after which they are dried at 100 °C for 30 min. This dipping/drying operation is repeated 3 times under the same conditions, with a 30-min wait time between cycles. The resulting samples were then heat-treated at 450 °C for 30 min at a 1 °C/min heat rate.

Bioglass synthesis

Bioactive glass (58S (58%) SiO₂ (37%) CaO (5%) P₂O₅) was synthesized using the evaporation-induced self-

Table 1 Chemical composition of the surgical 316L SS powder

Element	Fe	C	Si	Mn	P	S	Cr	Ni	Mo	N	Cu	O
Minimum	Balance	0	0	0	0	0	16	11	2	0	0	0
Actual	Balance	0.024	0.45	1.22	<0.005	0.005	16.92	12.08	2.4	0.01	0.01	0.03
Maximum	Balance	0.03	0.75	2	0.025	0.01	18	13	3	0.1	0.5	0.1

Fig. 1 a, b The SS alloy rhombic dodecahedron lattice structure. c, d Model sample part e, f: the orthopedic implant.

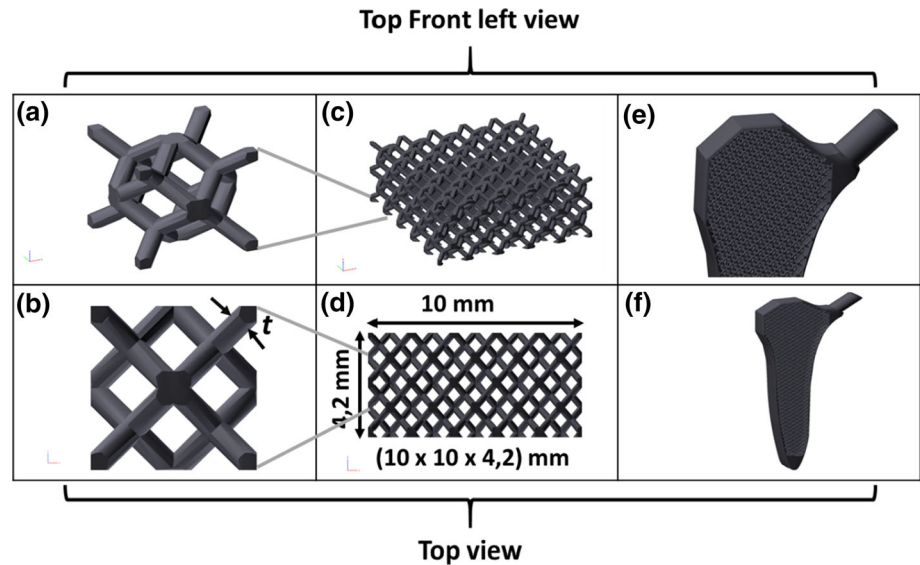


Table 2 SLM process parameters used in this study

Parameters process	General	
Layer thickness	50 μm	
Base plate temperature	80 $^{\circ}\text{C}$	
Atmosphere	Nitrogen, 12 mbar overpressure	
	Border	Volume
Scanning strategy	–	Stripes
Hatch spacing (h)	0.08 mm	0.12 mm
Average scanning speed (v)	300 mm/s	700 mm/s
Power laser (P)	100 W	275 W
Volumetric laser energy density (E_v)	83.33 J/mm ³	65.48 J/mm ³

assembly (EISA) method as reported previously [35, 36]. 5 g of non-ionic surfactant L-81 was added to a mixture of ethanol and 0.5 M HCl. The solution was stirred for 30 min before the addition in this order: TEOS (4,8 g), TEP and calcium nitrate (3,4 g) as precursors for silicate, phosphorus and calcium, respectively. The resulted solution was kept under continuous agitation for 1 day. The sol was transferred to petri dishes to undergo EISA process, followed by heat treatment at 40 $^{\circ}\text{C}$ for 7 days, to ensure the evaporation of ethanol and self-assembly of surfactant molecules. The dried gel was calcined at 600 $^{\circ}\text{C}$ for 6H to obtain the final bioglass denoted as “58S”.

Bioglass suspension preparation and coating

The 316L-SS cellular structures implants were dip-coated in a 58S glass particles suspension. This suspension was prepared by ultrasonic dispersion of 58S bioactive glass particles in ethanol, at a concentration of 5% and 10% (w/v). Both untreated (CS3–CS4) and silicate-coated (CS5, CS6) structures were immersed for 15 min in the 58S glass suspension, followed by a heat treatment at 450 $^{\circ}\text{C}$ for 30 min. Table 3 lists all prepared samples with a brief description of coating procedures.

In vitro Bioactivity test in SBF medium

The biological activity of the *as*-produced bioglass 58S in acellular medium was evaluated in SBF after 6H, 16H, 1D, 3D and 7D of immersion, with a static mode without changing the environment after each period of immersion, in order to evaluate its ability to deposit new apatite layers. *In vitro* bioactivity tests of the aforementioned cellular structures (Table 2) were performed before and after BG coating, using a 7-day immersion period in SBF medium. This period was selected based on results showing significant bioactivity for these bioglass powders. This bioactivity was appraised using procedures described in the previous studies [37]. The SBF solution was prepared according to the previous reports [38, 39].

Table 3 Description of cellular structures studied

Acronym Sample	CS1	CS2	CS3	CS4	CS5	CS6
Description	316L-SS/ SLM	316L-SS/ SLM-SiO ₂ with SiO ₂ layer pretreatment	316L-SS/ SLM Coated with 5% 58S-BG	316L-SS/ SLM Coated with 10% 58S-BG	316L-SS/ SLM-SiO ₂ Coated with 5% 58S-BG	316L-SS/ SLM-SiO ₂ Coated with 10% 58S-BG

Bioglass and Scaffold Characterization

Prior to selective laser melting manufacturing, the powder size distribution and shape factor were established via dynamic image analysis, using a Camsizer X2 (Retsch, Germany) equipped with dual camera technology. Structural features of calcined and coated samples were assessed with X-ray diffraction (XRD), Fourier transform infrared spectroscopy (FTIR) and inductively coupled plasma atomic emission spectroscopy (ICP-AES). XRD patterns were collected on an X-pert X-ray diffractometer using 0.02 as a step size and 180 s as a step time. The CuK α was used as X-ray radiation and was generated under voltage and current of 45 kV and 40 mA, respectively. Data were collected for 2 θ values ranging from 10° to 70°. The FTIR spectra of the bioactive glass series were obtained in attenuated total reflection mode (ATR) using a Nicolet IS50 spectrometer. Transmission spectra of specimens were obtained between 400 and 4000 cm⁻¹ at a resolution of 4 cm⁻¹. Analysis of the chemical composition of powders was carried out by inductively coupled plasma atomic emission spectroscopy (ICP-AES), using a Jobin Yvon Horiba Ultima 2 apparatus. Results were averaged from three repeated measurements. SEM micrographs coupled to energy-dispersive X-ray spectroscopy (SEM/EDS) were obtained using an IEM11⁺Inovenco SEM microscope under high vacuum mode and a voltage of 15 kV, to assess the structural and morphological change of various bioglass powders, and the growth of the new apatite layer on coated specimens. Gold metallization was used on bioglass powders sample to reduce surface charging, while lattice structures were analyzed without metallization.

Results and Discussion

Metallic powders and as-printed SLM cellular structures

The powder material used to print the sample parts and the porous orthopedic implants consist of gas atomized particles, ranging from 10 to 90 μm in diameter (see Fig. 2a). Particle size distribution of the 316L-SS metal powder used in this work is presented in Fig. 2a. The volume-based d_{10} , d_{50} , d_{90} values are summarized in Table 4. The average particle size is 34.6 μm , with 90% of the particles having a diameter of 51.3 μm or less. Particle morphology was found to be roughly spherical from SEM observations (Fig. 2b). The SEM micrographs revealed the presence of small particles partially covering the surface of the larger ones.

Analysis of the particle size distribution (Fig. 2a) reveals an asymmetric trend toward finer grains. The ratios of d_{50}/d_{10} and d_{90}/d_{10} displayed in the last two columns of Table 4 give characteristic parameters of the suitability of metal powder granulometry used in selective laser melting production according to the Karapatis criteria [40]. These conditions are as follows:

$$d_{90} < t_{\text{layer}}; \quad d_{50}/d_{10} \geq 10 \quad \text{and} \quad d_{90}/d_{10} \leq 19$$

where t_{layer} is the layer thickness, d_{10} , d_{50} and d_{90} are the diameter at 10%, 50% and 90% of the powder population. The first requirement between d_{90} and t_{layer} can be considered to be closely met for the studied powder. The $d_{50}/d_{10} \geq 10$ condition has not been met in the present case, while the third condition ($d_{90}/d_{10} \leq 19$) is achieved. This makes it possible to print with an effective layer of particles, where the smaller particles bridge the gaps between the large ones, thus ensuring a proper packing behavior. The use of a powder with a larger d_{90} often results in parts with rough and non-uniform surfaces. Similar results were also obtained in another study on

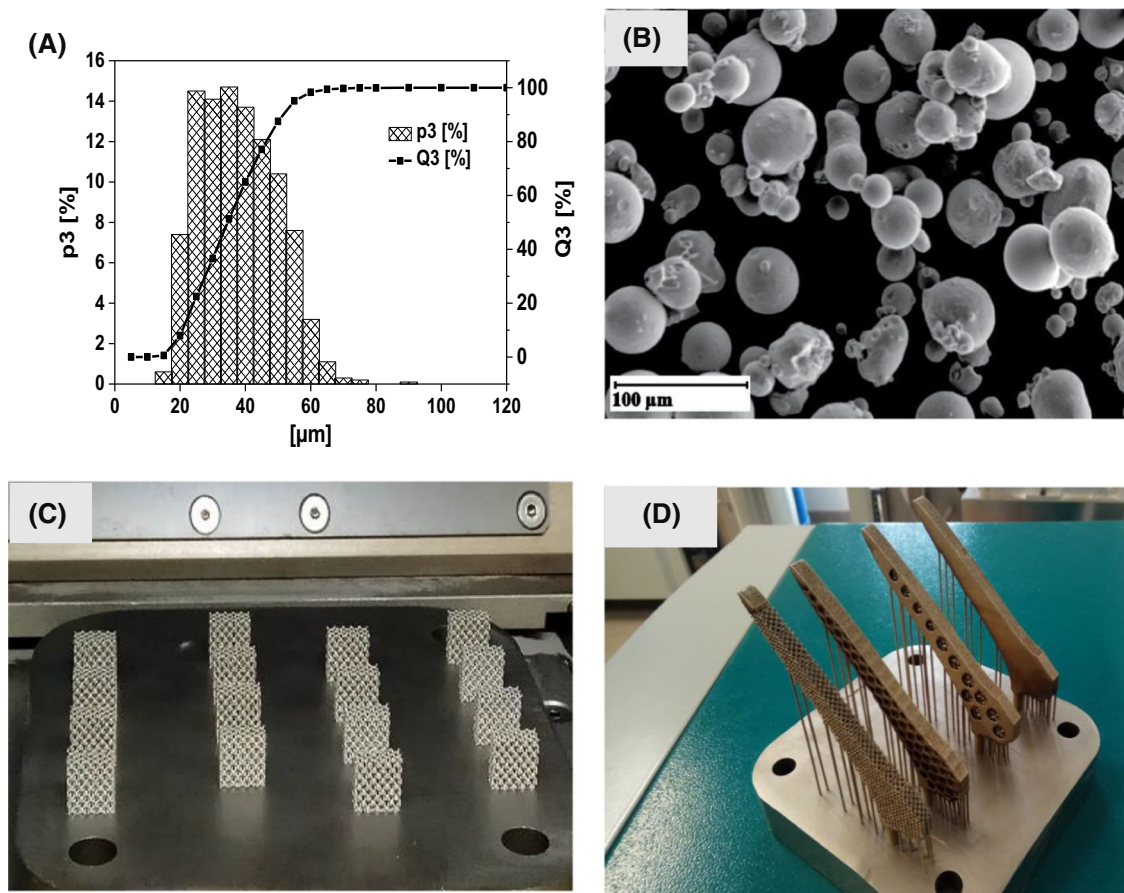


Fig. 2 a The particle size distribution (differential and cumulative); b SEM micrograph of 316L-stainless steel powders; as-printed sample parts c and orthopedic implants d still on the build plate.

Table 4 Characteristics values for the particle size distribution

Metal powders	d_{10} (μm)	d_{50} (μm)	d_{90} (μm)	d_{50}/d_{10}	d_{90}/d_{10}
316L-SS	20.8	34.6	51.3	1.66	2.46

meeting the Karapatis criteria and grain size distribution of 316L-SS [41].

Characterization of 58S bioglass

The diffraction patterns of 58S bioglass powder are shown in Fig. 3a. From this figure, it is clearly seen that samples calcined at 600 °C in air exhibit an amorphous phase containing pseudo-crystalline phases of CaO and CaCO₃. Also present at 29° [2θ] are the characteristic band of calcite, the crystalline phase of calcium carbonate CaCO₃, and small peaks of crystalline calcium oxide (CaO) at 32°, 39° and 53.7° [2θ]. Similar results were observed by Li and Mozafari works [42, 43]. As observed, the increase to

a heat treatment temperature above the crystallization temperature yields a crystalline structure instead of an amorphous one [44]. This may explain the amorphous nature of 58S bioglass produced by EISA method, which is accompanied by a small crystalline fraction. This combination is key to enhance many properties such as bioactivity and biocompatibility. A recent study concluded that increasing the sintering temperature can enhance the crystallinity degree, leading in turn to an optimal biomineralization [45].

Intermolecular interactions of bioglass particles were also examined by FTIR analysis (Fig. 3b). The peaks at 3373 and 1636 cm⁻¹, assigned to O–H bands, are explained by the presence of adsorbed water in the samples [44]. Traces of crystalline CaCO₃ and

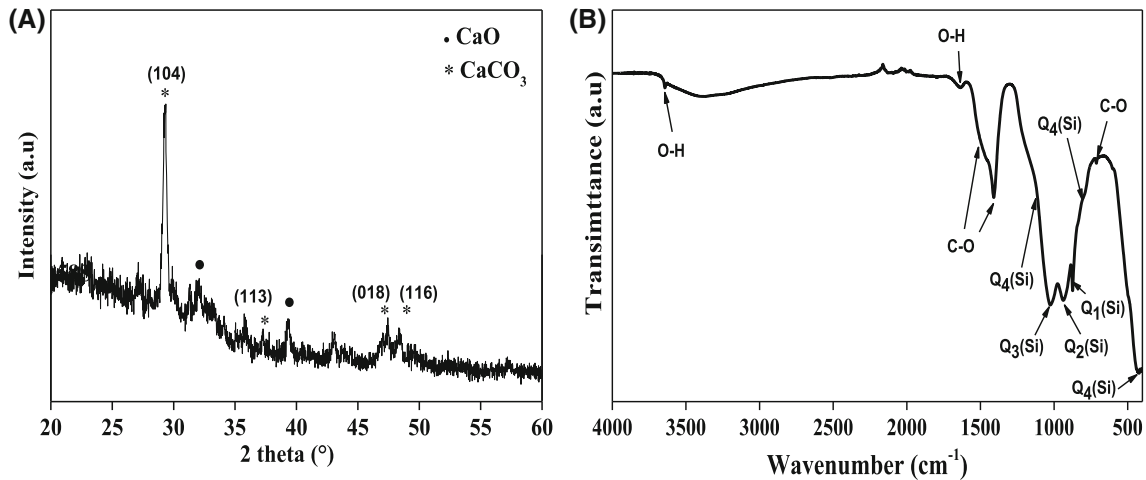


Fig. 3 XRD patterns (a) and FTIR spectra (b) of bioactive glass 58S calcined at 600 °C for 6H in air atmosphere.

CaO seen in XRD analysis are confirmed by FTIR analysis with the presence of C–O bands at 712, 1410 and 1521 cm^{-1} [46]. The dominant phase of bioglass is given by the characteristic bands of silica. This includes the deformation vibrations of Si–O–Si found at 436, 811 and 1100 cm^{-1} , which is the symmetric bending of SiO_4 tetrahedrons defined as Q^4 (Si) in Fig. 3b, and bands at 875, 935 and 1028 cm^{-1} which are the stretching vibrations of Si–O–Si bonds in the Q^1 (Si), Q^2 (Si) and Q^3 (Si) tetrahedrons, respectively. These latter consisted of 1, 2 and 3 bridging oxygen atoms [47, 48]. Bioglass samples were analyzed by ICP-AES for chemical composition (Table 5), with results consistent with expected composition.

Evaluation of the 58S bioglass particles morphology distribution and elemental analysis was carried out by scanning electron microscopy (Fig. 4). SEM imagery shows a clear presence of both crystallized and amorphous phases, where bioglass exists as irregular micro-/nanoparticles. The 58S BG micro-particles exhibit an irregular shape with a diameter varying between 28 and 38 μm . Nano-grains of 58S BG were regular and spherical, having an approximate size of 146 nm. These nano-grains are responsible for the high tendency of the powder to agglomerate [49]. The same results were observed by

Table 5 Quantitative analysis of 58S bioglass measured by ICP-AES

Constituents	SiO_2 mol%	CaO mol%	P_2O_5 mol%
Molar percentage	57.24 ± 0.08	36.57 ± 0.06	3.24 ± 0.09

Gong and al. [50]. The energy-dispersive spectroscopy (EDS) spectrum indicates that our powders are mainly composed of Si, Ca, P and C, confirming the chemical composition of the 58S bioglass. The conductive coating layer deposited on the sample prior to analysis explains the presence of gold (Au), while copper (Cu) and aluminum (Al) are explained by the sample holder used.

Characterization of the BG coating

SEM micrographs of the lattice structures before and after bioglass coating (CS1–CS6), and their corresponding EDS analysis are presented in Fig. 5. CS1 is the *as-fabricated* structure without any modification, where a high density and no surface porosity can be observed. The lattice structure exhibits a non-uniform and rough surface with a high aspect of balling effect. This phenomenon is frequently observed in *laser-based* additive manufacturing and results from a complex physical metallurgical process. It occurs mostly for lattice structures with very thin walls and can be explained by instability of the melt pool during lasing [51]. SEM imaging reveals a large amount of small-sized spherical balls averaging 40 μm . (*The average diameter was determined using Image J 1.52, a software on a population of 40 balls.*) Melt pool instability also results in solidified spheres found on various sides of the printed sample because of small droplets splashing. Using a low scan speed could lead to an energy increase in the melt pool, increasing the balling effect in lattice structures. The difference between the melt pool created during hatches

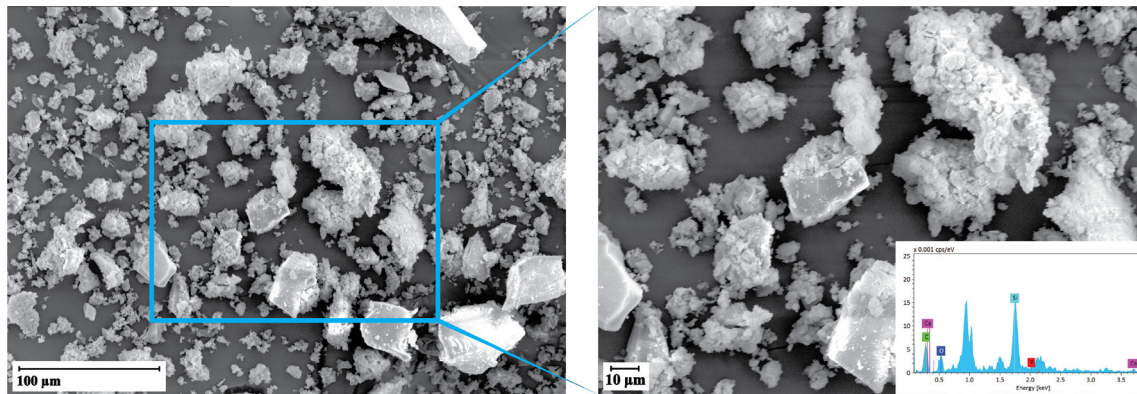


Fig. 4 SEM micrograph and EDS pattern of the synthesized 58S bioglass particles heat treated at 600 °C.

scanning and during contour scanning can explain the appearance of spherical balls and irregular surface [51, 52]. Peaks of Co, Ni, Fe, C, and Si found during EDS analysis are typical of 316L stainless steel.

SEM of lattice structures treated with SiO₂ (CS₂) (Fig. 5) revealed micro-cracks formed during heat treatment to remove water molecules. SEM of CS3–CS6 samples revealed that the impregnation rate of 58S bioglass is influenced by the surface (with or without prior silicate layer treatment) as well as the concentration of suspension used for coating. EDS spectra of impregnated samples show additional peaks of P, Ca, O and Si (with a more pronounced intensity for Si), confirming the presence of a layer of bioglass coating. Surface morphology of the coated sample is influenced by the concentration of bioglass in suspension. While a 10 wt% suspension yields a homogenous and dense surface with some micropores observed, the 5 wt% suspension results in a non-uniform and rough appearance. Formation of micro-cracks might be explained by layer shrinkage during sintering. This is something favorable for the osseointegration process because the presence of an interconnected open porous structure would help achieve the vascularization necessary for the growth of new tissues [53, 54] inside and on the surface of the hip implant. By pretreating the lattice structure with a silicate layer, followed by a 58S bioglass impregnation, homogenous and dense porous composite materials can be obtained. This is advantageous to address issues of stress shielding and metal ions release resulting from a degradation of the metal implant. This observation is in full agreement and approved by Sidane et al. studies; they explored the hydroxyapatite (HA)-TiO₂-SiO₂-coating on 316L

stainless steel, morphological and mechanical properties. They found that the silica layer enhanced the attachment of the TiO₂ and HA phase through the Si–OH hydroxyl groups, thus signifying a perfection in the corrosion resistance, bonding strength, elastic modulus and hardness of the coated 316 L SS essential for the hard tissue applications [55, 56].

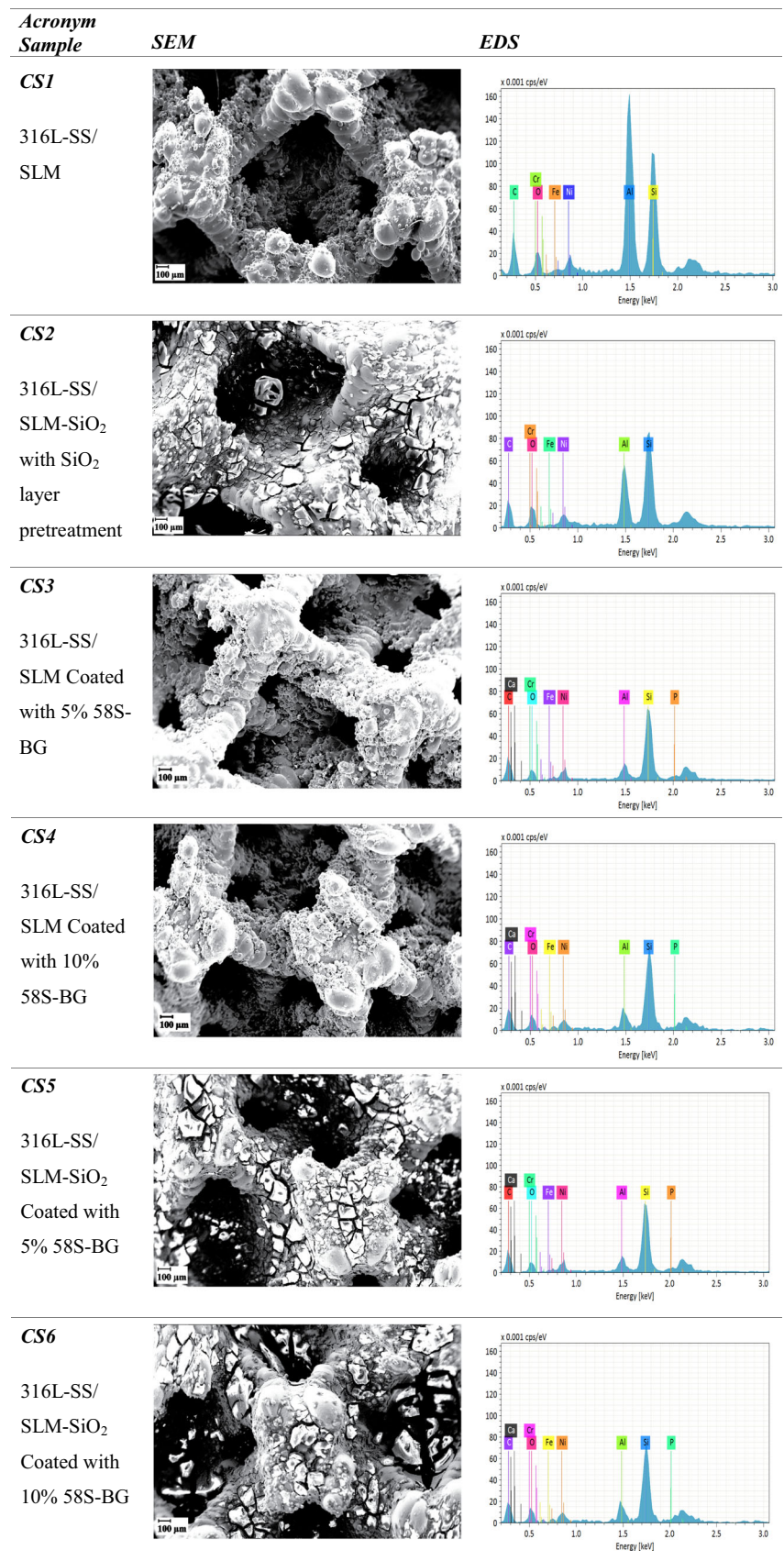
Assessment of the In Vitro Bioactivity

Bioglass powders bioactivity in SBF medium

The XRD patterns of bioglass powders before and after soaking in SBF medium for different periods of time (16 h to 7 days) are shown in Fig. 6a. While immersion tests were conducted from 16 h to 7 days, observed morphological changes were used as selection criteria. XRD spectra at 16 h start exhibiting the characteristics of hydroxyapatite (HA) at 25, 88° and 31,77° [2θ], becoming more pronounced after 7 days of immersion [43]. These reflections are related to (002) and (211) plans diffraction according to the standard data base (*PDF card No. 09-0432*) [57]. In addition to HA, peaks of crystallized phases CaCO₃ and CaO can be observed in the samples, becoming less noticeable with time. This confirms that the crystallized phases do not prevent formation of a new apatitic layer. This enhanced reactivity might be caused by the dissolution of CaCO₃ and CaO during immersion as confirmed from Dehaghani et al. work [58].

The FTIR spectra of powders after immersion in SBF solution for 16 h and 7 days are presented in Fig. 6b. It took only 6 h of soaking 58S bioglass in SBF to observe new P–O bands, a sign of apparent bioactivity [59]. These results are in agreement with

Fig. 5 SEM and EDS of the as printed and produced sample parts.



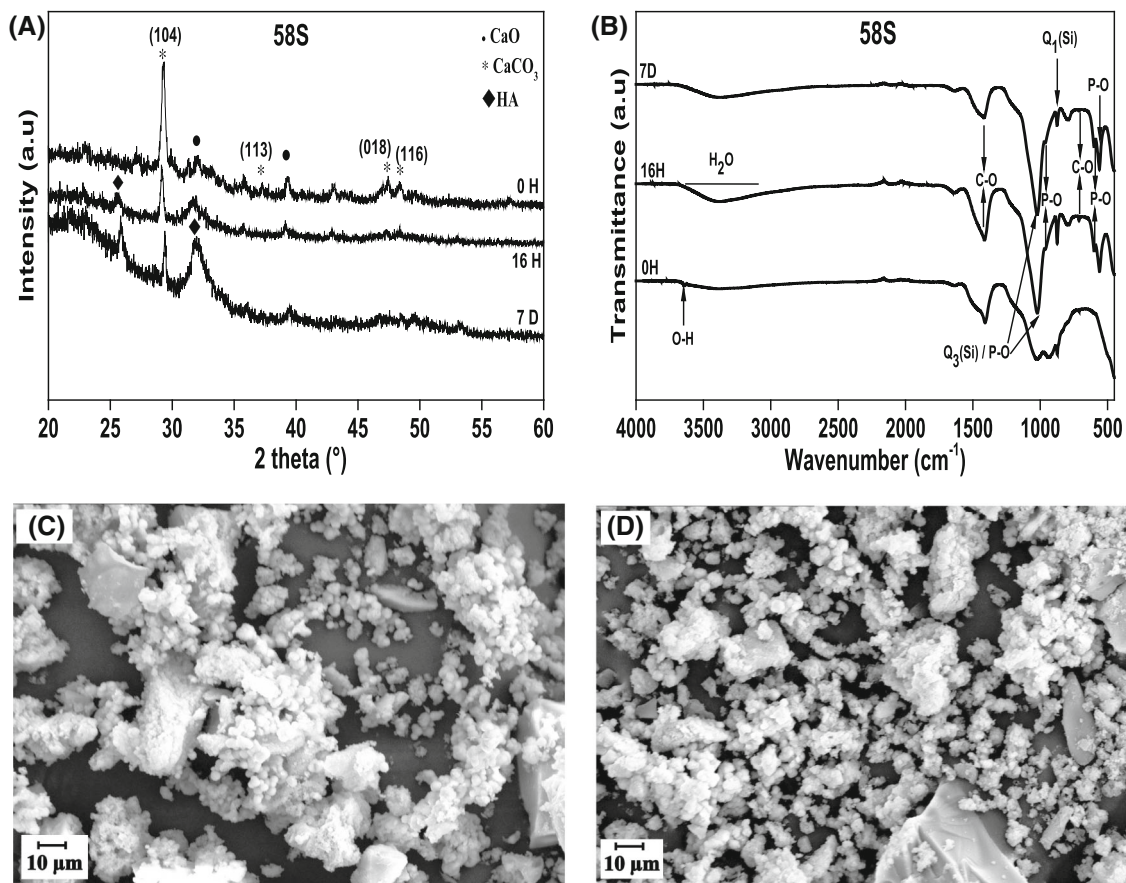


Fig. 6 XRD patterns (a) and infrared spectra (b) of the 58S bioglass after immersion in SBF for different periods of time 16H (c) and 7 days (d).

XRD observations (Fig. 6a). Functional bands of Si–O, Si–O–Si and C–O, already present before immersion, are still found after soaking in SBF medium. Their intensity, however, decrease with immersion time as observed with the carbonate bands at 1419 and 715 cm^{-1} . This can be explained by dissolution of crystalline phases (CaCO_3 , CaO). Phosphate absorption in the crystalline state is confirmed by the formation of very well-defined bands around 570, 609, 968 and 1020 cm^{-1} [58]. The vibration around 964 cm^{-1} , related to Q_2 (Si), became more apparent after 16 h of immersion and overlaps the characteristic band of P–O function at 968 cm^{-1} . A similar modification occurred for the Q_3 (Si) vibration at 1028 cm^{-1} and phosphate group at $\sim 1020 \text{ cm}^{-1}$. This is in line with the steps discussed by Hench to explain the bioglass' bioactivity process [47].

The XRD and FTIR analysis thus confirmed the acellular bioactivity of the produced bioglass 58S by EISA method. The biological activity of the 58S bioglass was also confirmed by SEM carried out on

samples immersed in SBF, where deposits of a new apatitic phase were observed on the surface of the bioglass powders (Fig. 6c, d). The glass surface was completely changed because of the reactions occurring between the SBF medium and glass surface. These are a significant sign of the produced “58” glass bioactivity in acellular medium. After 16 h of soaking, the glass surface is totally covered with a homogenous and dense particle with a spherical shape. Increasing the immersion period to 7 days yields a more visible and larger deposited layer because of the enhanced crystallization of hydroxyapatite (HA) particles with a spherical shape [44, 60]. These results are in agreement with XRD and FTIR analysis, demonstrating that “58S” bioglass possesses a good apatite-forming activity.

Bioactivity of the coated 3D-sample pieces

To estimate the in vitro bioactivity of coated samples, the surface morphologies were observed by SEM for

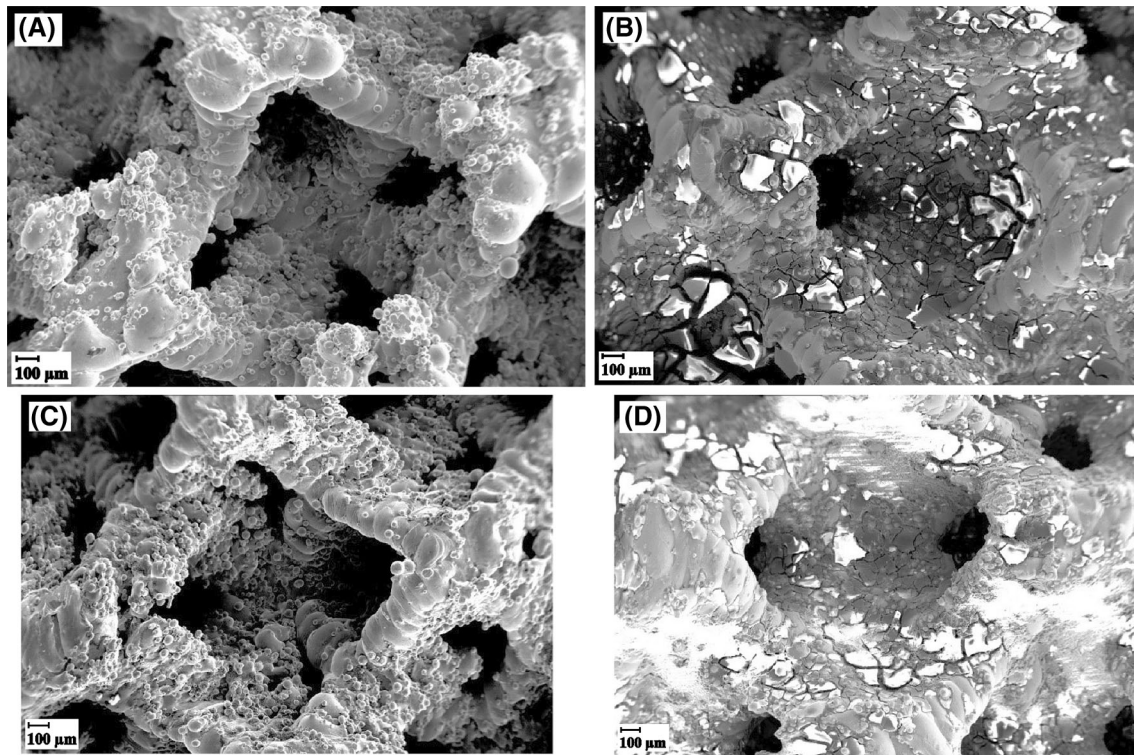


Fig. 7 SEM micrographs of CS1, CS2, CS4 and CS6 after a 7-day immersion in SBF.

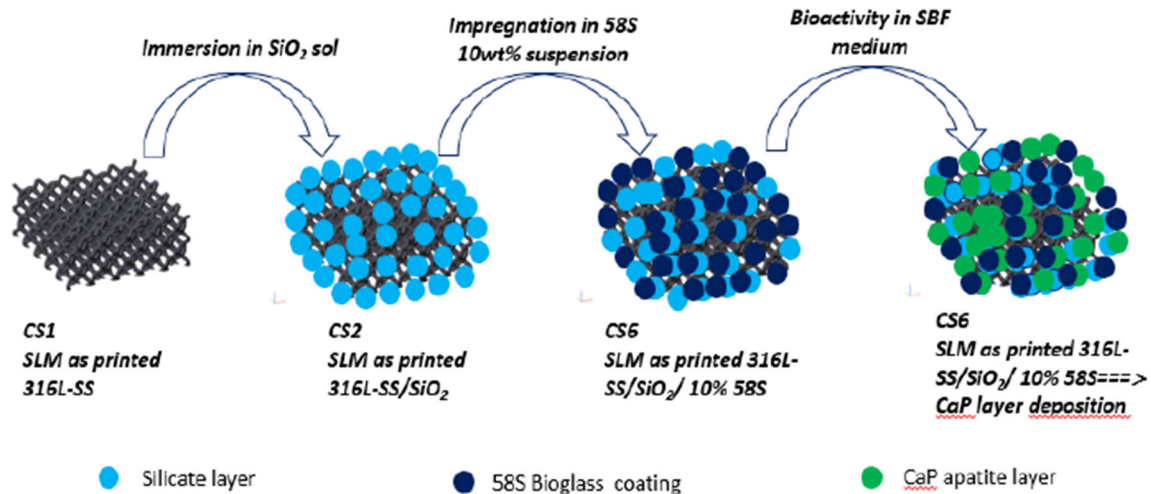
selected samples showing the densest and homogeneous coating (CS1, CS2, CS4 and CS6) (Fig. 7). The *in vitro* bioactivity test was carried out in SBF medium for 7 days of immersion to ensure the chemical reaction of bioglass particles with the surrounding body fluid. This is considered as a preliminary signal of bioactivity in the human body [54]. The CS1 sample, used as reference for this test, shows no growth on its surface. The same behavior is observed for the sample part with bioglass coating after impregnation. The *in vitro* test revealed that formation of a new layer of semicrystalline hydroxyapatite on the substrate surface is induced only for pretreated samples parts with SiO₂ layers and bioglass suspension. Growth was enhanced with the addition of bioglass coating. The CS6 sample showed a very important agglomeration of particles on the surface when compared to CS2 sample. Bioactivity of 58S bioglass enabled the formation of hydroxyapatite after only 16H of immersion period, as proved in Fig. 6.

It has already been established that formation of apatite occurs through ion exchange between the bioglass coating and SBF solution, with the SiO₂ layer being a crucial pretreatment to stainless steel parts to achieve enhanced biological activity (Scheme 1). Our

method of achieving porous metal parts coated with dense layers of bioglass shows promising bioactivity results. This approach can serve as a new generation of hybrid porous hip implants with an architecture mimicking the human bone.

Conclusion

In the present study, 316L stainless steel (316L-SS) lattice structures based on rhombic dodecahedron unit cell with a relative density of 20% were designed and produced using selective laser melting (SLM) method. The resulting structures were then coated with 58S bioactive glass to enhance bioactivity. This hybrid structure exhibits the functionalities required to be used in a new generation of hip implant with reduced stiffness and weight. This would yield increases in bone density inside and around the implant because of the homogeneous bioactive glass layer coating the metallic structure. Quality of this layer is firmly dependent on the chemical surface treatment performed before impregnation. This bioglass layer will improve the *in vitro* bioactivity in SBF medium. Thanks to the high specific surface of the



Scheme 1 Scheme of different steps of bioglass coating process on metallic porous parts.

metallic framework structures, other elements can be added such as growth factors, anti-inflammatories and antibiotics to further improve the biologic properties of these new structures.

Acknowledgements

Authors address their acknowledgements to the National Center of Scientific and Technological Research, CNRST (Rabat, Morocco), the Regional Council Fes-Meknes and the Euromed University of Fes for supporting the present study.

References

- [1] Smith MC, Ben-Shlomo Y, Dieppe P, et al (2017) Rates of hip and knee joint replacement amongst different ethnic groups in England: an analysis of National Joint Registry data. *Osteoarthritis Cartilage* 25:448–454. <https://doi.org/10.1016/j.joca.2016.12.030>
- [2] Culliford D, Maskell J, Judge A et al (2015) Future projections of total hip and knee arthroplasty in the UK: results from the UK clinical practice research datalink. *Osteoarthritis Cartilage* 23:594–600. <https://doi.org/10.1016/j.joca.2014.12.022>
- [3] Lübbeke A, Silman AJ, Barea C et al (2018) Mapping existing hip and knee replacement registries in Europe. *Health Policy (N Y)* 122:548–557. <https://doi.org/10.1016/j.healthpol.2018.03.010>
- [4] Kurtz S, Ong K, Lau E et al (2007) Projections of primary and revision hip and knee arthroplasty in the United States from 2005 to 2030. *J Bone Jt Surg Ser A* 89:780–785. <https://doi.org/10.2106/JBJS.F.00222>
- [5] Ginebra M-P, Espanol M, Maazouz Y et al (2018) Bioceramics and bone healing. *EFORT Open Rev* 3:173–183. <https://doi.org/10.1302/2058-5241.3.170056>
- [6] Strumza E, Yeheskel O, Hayun S (2019) The effect of texture on the anisotropy of thermophysical properties of additively manufactured AlSi10Mg. *Addit Manuf* 29:100762. <https://doi.org/10.1016/j.addma.2019.06.013>
- [7] Gumbleton R, Cuenca JA, Klemencic GM et al (2019) Evaluating the coefficient of thermal expansion of additive manufactured AlSi10Mg using microwave techniques. *Addit Manuf* 30:100841. <https://doi.org/10.1016/j.addma.2019.100841>
- [8] Gao C, Peng S, Feng P, Shuai C (2017) Bone biomaterials and interactions with stem cells. *Bone Res* 5:1–33. <https://doi.org/10.1038/boneres.2017.59>
- [9] Yan Q, Dong H, Su J et al (2018) A review of 3D printing technology for medical applications. *Engineering* 4:729–742. <https://doi.org/10.1016/j.eng.2018.07.021>
- [10] Zadpoor AA, Malda J (2017) Additive manufacturing of biomaterials, tissues, and organs. *Ann Biomed Eng* 45:1–11. <https://doi.org/10.1007/s10439-016-1719-y>
- [11] Liu F, Mao Z, Zhang P et al (2018) Functionally graded porous scaffolds in multiple patterns: new design method, physical and mechanical properties. *Mater Des* 160:849–860. <https://doi.org/10.1016/j.matdes.2018.09.053>
- [12] Ibrahim MZ, Sarhan AAD, Yusuf F, Hamdi M (2017) Biomedical materials and techniques to improve the tribological, mechanical and biomedical properties of orthopedic implants—a review article. *J Alloys Compd.* <https://doi.org/10.1016/j.jallcom.2017.04.231>

- [13] Mahmoud D, Elbestawi M (2017) Lattice structures and functionally graded materials applications in additive manufacturing of orthopedic implants: a review. *J Manuf Mater Process* 1:13. <https://doi.org/10.3390/jmmp1020013>
- [14] Harrysson OLA, Cansizoglu O, Marcellin-Little DJ et al (2008) Direct metal fabrication of titanium implants with tailored materials and mechanical properties using electron beam melting technology. *Mater Sci Eng C* 28:366–373. <https://doi.org/10.1016/j.msec.2007.04.022>
- [15] Murr LE, Gaytan SM, Martinez E et al (2012) Next generation orthopaedic implants by additive manufacturing using electron beam melting. *Int J Biomater*. <https://doi.org/10.1155/2012/245727>
- [16] Yuan L, Ding S, Wen C (2019) Additive manufacturing technology for porous metal implant applications and triple minimal surface structures: a review. *Bioact Mater* 4:56–70. <https://doi.org/10.1016/j.bioactmat.2018.12.003>
- [17] Pantoja M, Velasco F, Abenobar J, Martinez MA (2019) Development of superhydrophobic coatings on AISI 304 austenitic stainless steel with different surface pretreatments. *Thin Solid Films* 671:22–30. <https://doi.org/10.1016/j.tsf.2018.12.016>
- [18] Fathi MH, Doost Mohammadi A (2008) Preparation and characterization of sol–gel bioactive glass coating for improvement of biocompatibility of human body implant. *Mater Sci Eng A* 474:128–133. <https://doi.org/10.1016/j.msea.2007.05.041>
- [19] Fathi MH, Doostmohammadi A (2009) Bioactive glass nanopowder and bioglass coating for biocompatibility improvement of metallic implant. *J Mater Process Technol* 209:1385–1391. <https://doi.org/10.1016/j.jmatprotec.2008.03.051>
- [20] Omar SA, Ballarre J, Ceré SM (2016) Protection and functionalization of AISI 316 L stainless steel for orthopedic implants: hybrid coating and sol gel glasses by spray to promote bioactivity. *Electrochim Acta* 203:309–315. <https://doi.org/10.1016/j.electacta.2016.01.051>
- [21] Al-Rashidy ZM, Farag MM, Ghany NAA et al (2017) Aqueous electrophoretic deposition and corrosion protection of borate glass coatings on 316 L stainless steel for hard tissue fixation. *Surfaces Interfaces* 7:125–133. <https://doi.org/10.1016/j.surfin.2017.03.010>
- [22] Deposition AL (2010) Atomic layer deposition. *Chem Rev* 110:111–131. <https://doi.org/10.1021/cr900056b>
- [23] George SM (2010) Atomic layer deposition: an overview. *Chem Rev* 110:111–131. <https://doi.org/10.1021/cr900056b>
- [24] Putkonen M, Sajavaara T, Rahkila P et al (2009) Atomic layer deposition and characterization of biocompatible hydroxyapatite thin films. *Thin Solid Films* 517:5819–5824. <https://doi.org/10.1016/j.tsf.2009.03.013>
- [25] Wang D, Bierwagen GP (2009) Sol–gel coatings on metals for corrosion protection. *Prog Org Coat* 64:327–338. <https://doi.org/10.1016/j.porgcoat.2008.08.010>
- [26] Houmard M, Nunes EHM, Vasconcelos DCL et al (2014) Correlation between sol–gel reactivity and wettability of silica films deposited on stainless steel. *Appl Surf Sci* 289:218–223. <https://doi.org/10.1016/j.apsusc.2013.10.137>
- [27] Pourhashem S, Afshar A (2014) Double layer bioglass-silica coatings on 316L stainless steel by sol–gel method. *Ceram Int* 40:993–1000. <https://doi.org/10.1016/j.ceramint.2013.06.096>
- [28] Luo J, Jia X, Gu R et al (2018) 316L stainless steel manufactured by selective laser melting and its biocompatibility with or without hydroxyapatite coating. *Metals (Basel)* 8:548. <https://doi.org/10.3390/met8070548>
- [29] Melo-Fonseca F, Lima R, Costa MM et al (2018) 45S5 BAG-Ti₆Al₄V structures: The influence of the design on some of the physical and chemical interactions that drive cellular response. *Mater Des* 160:95–105. <https://doi.org/10.1016/j.matdes.2018.08.056>
- [30] Yamamoto A, Kohyama Y, Kuroda D, Hanawa T (2004) Cytocompatibility evaluation of Ni-free stainless steel manufactured by nitrogen adsorption treatment. *Mater Sci Eng C* 24:737–743. <https://doi.org/10.1016/j.msec.2004.08.017>
- [31] Zadpoor AA (2019) Additively manufactured porous metallic biomaterials. *J Mater Chem B* 7:4088–4117. <https://doi.org/10.1039/c9tb00420c>
- [32] Gopi D, Ramya S, Rajeswari D, Kavitha L (2013) Corrosion protection performance of porous strontium hydroxyapatite coating on polypyrrole coated 316L stainless steel. *Colloids Surfaces B Biointerfaces* 107:130–136. <https://doi.org/10.1016/j.colsurfb.2013.01.065>
- [33] He L, Wang Z, Sheath P et al (2015) Growth of nano-textured graphene coatings across highly porous stainless steel supports towards corrosion resistant coatings. *Carbon*. <https://doi.org/10.1016/j.carbon.2015.02.042>
- [34] Manakari V, Parande G, Gupta M (2016) Selective laser melting of magnesium and magnesium alloy powders: a review. *Metals* 7:2
- [35] Yan X, Yu C, Zhou X et al (2004) Highly ordered mesoporous bioactive glasses with superior in vitro bone-forming bioactivities. *Angew Chemie Int Ed* 43:5980–5984. <https://doi.org/10.1002/anie.200460598>
- [36] Brinker CJ, Lu Y, Sellinger A, Fan H (2010) ChemInform abstract: evaporation-induced self-assembly: nanostructures made easy. *ChemInform*. <https://doi.org/10.1002/chin.199928288>

- [37] Tabia Z, El Mabrouk K, Bricha M, Nouneh K (2019) Mesoporous bioactive glass nanoparticles doped with magnesium: drug delivery and acellular in vitro bioactivity. *RSC Adv*. <https://doi.org/10.1039/C9RA01133A>
- [38] Bricha M, Belmamouni Y, Essassi EM et al (2013) Hydrothermal synthesis and appraisal of Mg-doped hydroxyapatite nanopowders. *J Biomater Tissue Eng* 3:570–580. <https://doi.org/10.1166/jbt.2013.1120>
- [39] Belmamouni Y, Bricha M, Ferreira J, El Mabrouk K (2015) Hydrothermal synthesis of Si-doped hydroxyapatite nanopowders: mechanical and bioactivity evaluation. *Int J Appl Ceram Technol* 12:329–340. <https://doi.org/10.1111/ijac.12210>
- [40] Karapatis N, Egger G (1999) Optimization of powder layer density in selective laser sintering. *Int Solid Free Fabr Symp*. <https://doi.org/10.26153/tsw/746>
- [41] Zegzulka J, Gelnar D, Jezerska L et al (2018) Internal friction angle of metal powders. *Metals (Basel)* 8:255. <https://doi.org/10.3390/met8040255>
- [42] Li XN, Chen XM, Hu WL (2009) In Situ synthesis and characterization of β -tricalcium phosphate/Na doped 58S bioglass composite by sol–gel technique. *Mater Sci Forum* 610–613:1278–1283. <https://doi.org/10.4028/www.scientific.net/msf.610-613.1278>
- [43] Mozafari M, Mozartzadeh F, Tahriri M (2010) Investigation of the physico-chemical reactivity of a mesoporous bioactive SiO_2 -CaO- P_2O_5 glass in simulated body fluid. *J Non Cryst Solids* 356:1470–1478. <https://doi.org/10.1016/j.jnoncrysol.2010.04.040>
- [44] Liu Y, Xue K, YAO S, (2019) Structure, degradation and hydroxyapatite conversion of B-doped 58S bioglass and glass-ceramics. *J Ceram Soc Jpn* 127:232–241. <https://doi.org/10.2109/jcersj2.18206>
- [45] Chitra S, Bargavi P, Durgalakshmi D et al (2019) Role of sintering temperature dependent crystallization of bioactive glasses on erythrocyte and cytocompatibility. *Process Appl Ceram* 13:12–23. <https://doi.org/10.2298/pac1901012c>
- [46] Busca G, Lorenzelli V (1982) Materials chemistry infrared spectroscopic identification of species arising from reactive adsorption of carbon oxides on metal oxide surfaces. *Mater Chem* 7:89–126. [https://doi.org/10.1016/0390-6035\(82\)90059-1](https://doi.org/10.1016/0390-6035(82)90059-1)
- [47] Filgueiras MRT, La Torre G, Hench LL (1993) Solution effects on the surface reactions of three bioactive glass compositions. *J Biomed Mater Res* 27:1485–1493. <https://doi.org/10.1002/jbm.820271204>
- [48] Bui XV, Dang TH (2019) Bioactive glass 58S prepared using an innovation sol–gel process. *Process Appl Ceram* 13:98–103
- [49] Joughehdoust S, Manafi S (2012) Synthesis and in vitro investigation of sol–gel derived bioglass-58S nanopowders. *Mater Sci Pol* 30:45–52. <https://doi.org/10.2478/s13536-012-0007-2>
- [50] Gong W, Dong Y, Wang S et al (2017) A novel nano-sized bioactive glass stimulates osteogenesis via the MAPK pathway. *RSC Adv* 7:13760–13767. <https://doi.org/10.1039/c6ra26713k>
- [51] Gu D, Shen Y (2009) Balling phenomena in direct laser sintering of stainless steel powder: metallurgical mechanisms and control methods. *Mater Des* 30:2903–2910. <https://doi.org/10.1016/j.matdes.2009.01.013>
- [52] Mahmoud D, Elbestawi MA (2019) Selective laser melting of porosity graded lattice structures for bone implants. *Int J Adv Manuf Technol* 100:2915–2927. <https://doi.org/10.1007/s00170-018-2886-9>
- [53] Gopi D, Murugan N, Ramya S, Kavitha L (2014) Electrodeposition of a porous strontium-substituted hydroxyapatite/zinc oxide duplex layer on AZ91 magnesium alloy for orthopedic applications. *J Mater Chem B* 2:5531–5540. <https://doi.org/10.1039/c4tb00960f>
- [54] Arumugam MK, Hussein MA, Adesina AY (2019) In vitro corrosion and bioactivity performance of surface-treated Ti-20Nb-13Zr alloys for orthopedic applications. *Coatings* 9:344
- [55] Sidane D, Khireddine H, Yala S et al (2015) Morphological and mechanical properties of hydroxyapatite bilayer coatings deposited on 316L SS by sol–gel method. *Metall Mater Trans B Process Metall Mater Process Sci* 46:2340–2347. <https://doi.org/10.1007/s11663-015-0397-8>
- [56] Sidane D, Khireddine H, Bir F et al (2017) Hydroxyapatite- TiO_2 - SiO_2 -coated 316L stainless steel for biomedical application. *Metall Mater Trans A Phys Metall Mater Sci* 48:3570–3582. <https://doi.org/10.1007/s11661-017-4108-8>
- [57] Bricha M, Belmamouni Y, Essassi EM et al (2012) Surfactant-assisted hydrothermal synthesis of hydroxyapatite nanopowders. *J Nanosci Nanotechnol* 12:8042–8049. <https://doi.org/10.1166/jnn.2012.6664>
- [58] Taghian Dehaghani M, Ahmadian M, Fathi M (2015) Synthesis, Characterization, and Bioactivity Evaluation of Amorphous and Crystallized 58S Bioglass Nanopowders. *Int J Appl Ceram Technol* 12:867–874. <https://doi.org/10.1111/ijac.12293>
- [59] Kokubo T, Kushitani H, Sakka S et al (1990) Solutions able to reproduce in vivo surface-structure changes in bioactive glass-ceramic A-W3. *J Biomed Mater Res* 24:721–734. <https://doi.org/10.1002/jbm.820240607>
- [60] Xia W, Chang J (2008) Preparation, in vitro bioactivity and drug release property of well-ordered mesoporous 58S bioactive glass. *J Non Cryst Solids* 354:1338–1341. <https://doi.org/10.1016/j.jnoncrysol.2006.10.084>

Publisher's Note Springer Nature remains neutral with regard to jurisdictional claims in published maps and institutional affiliations.